



1 **Bushfire effects on soil properties and post-fire slope stability: the** 2 **case of the 2015 Wye River-Jamieson Track bushfire**

3 Yuanying Li¹, Akihiko Wakai¹, Susanga Costa²

4 ¹Graduate School of Science and Technology, Gunma University, Kiryu, 3768515, Japan

5 ²School of Engineering, Deakin University, Waurn Ponds, 3216, Australia

6 *Correspondence to:* Yuanying Li (t222c001@gunma-u.ac.jp)

7 **Abstract.** Bushfire is a destructive natural disaster that leads to vegetation loss and increased soil infiltration. Over a long
8 post-fire period, root death and reduced reinforcement decrease soil shear strength. During rainfall, shallow landslides in
9 burned areas become more frequent and widespread. This study focused on Wye River and Separation Creek in Australia,
10 affected by the 2015 Wye River-Jamieson Track bushfire. Ten months after the bushfire, multiple slope failures, including
11 the Paddy's Path landslide, occurred during heavy rains from 12 to 14 September 2016, disrupting the Great Ocean Road
12 connecting towns. This study aims to assess changes in slope stability during rainfall before and after the bushfire.
13 Controlled laboratory burning tests simulated bushfire effects on soil, resulting in changed soil properties after the fire:
14 increased permeability due to soil particle coarsening and reduced soil shear strength, especially cohesion. Considering the
15 changes in soil properties before and after the fire, a simplified hydrological numerical model for infiltration calculation was
16 employed to analyze time-dependent changes in groundwater level depth, surface water depth, and safety factor during
17 rainfall. Comparing pre- and post-fire results indicated higher susceptibility to shallow slope failures in burned areas, with
18 rapid rises in groundwater level and surface water acting as triggers. These findings enhance the understanding of landslide
19 triggering mechanisms in post-fire slopes and provide insights for mapping landslide susceptibility in bushfire-prone regions.

20 **1 Introduction**

21 Bushfires, also known as wildfires, are prevalent natural disasters that burn approximately 350 million ha globally each year
22 and are intensified by global warming and drought (Giglio et al., 2013). Particularly affected regions include the
23 Mediterranean, the Amazon, the western United States, and south-eastern Australia (Bowman et al., 2020). In Australia,
24 bushfires cost about 8.5 billion dollars annually, roughly 1.15 % of GDP, with severe fires in recent decades in Sydney,
25 Canberra, and Melbourne's exurban margins, causing significant losses of life, property, and forest resources (Ashe et al.,
26 2009). Bushfires not only cause immediate losses but also lead to lasting hydrological and geomorphological changes,
27 affecting soil physicochemical properties for months to years (Shakesby and Doerr, 2006). Post-fire vegetation losses
28 enhance infiltration, and reduce evapotranspiration, which elevate pore water pressure during rainfall and lower the threshold
29 for landslides (Staley et al., 2017). Lainas et al. (2016) reported that burned slopes require 20 %-30 % less rainfall to trigger



30 landslides compared to unburned ones. In the early 21st century, frequent rainfall-induced landslides and debris flows in
31 post-fire eucalypt forests in south-eastern Australia caused socioeconomic losses exceeding 60 million dollars (Freund et al.,
32 2017). Given the severe impact of these events, proactive assessment and mitigation strategies are crucial. Despite the
33 extensive damage and the clear need for preventive measures, studies on post-fire landslides remain limited (Abdollahi et al.,
34 2023).

35
36 Bordoloi and Ng (2020) indicated that despite the significant increase in the scale and frequency of bushfires, few studies
37 have addressed changes in soil mechanical properties and their impacts on post-fire slope stability. Identifying changes in
38 soil properties caused by bushfires remains challenging (Certini, 2005). Although it is acknowledged that changes in soil
39 physical and hydraulic properties due to fires are related to slope stability, the exact nature and extent of these changes
40 depend on factors such as fire severity, ecoregion, and time since the fire (Akin et al., 2023). In situ tests after bushfires have
41 proven instructive for collecting post-burn soil data, yet field investigations present various difficulties (Moody et al., 2013).
42 Unstable terrain and road closures immediately following bushfires hinder data collection. Fire sites may contain hazards
43 such as embers and unstable trees, posing risks to researchers (Brucker et al., 2022). Since soil properties are influenced by
44 factors such as topography, soil type, vegetation regimes, and climatic conditions, post-fire responses vary regionally,
45 leading to geographical variability in field survey results (Agbeshie et al., 2022). Additionally, the frequent absence of pre-
46 fire soil data restricts comparative analyses of slope stability before and after fires, making it challenging to accurately assess
47 the impact of changes in soil properties on post-fire stability.

48
49 Laboratory burning tests provide a highly controllable method for evaluating and quantifying changes in soil properties due
50 to bushfire impacts (Wieting et al., 2017). Previous laboratory studies have simulated bushfire effects on soils, examining
51 changes in properties such as particle size, saturated hydraulic conductivity, and infiltration capacity (Badia and Martí,
52 2003). Controlled settings in these tests overcome logistical challenges in field research, ensuring a safe working
53 environment and enabling precise control over experimental conditions and repeatability, which are difficult to achieve in
54 natural settings (Babrauskas and Grayson, 1990; Brucker et al., 2022). This approach allows for effective simulation of
55 diverse environmental conditions, such as various soil types, fire intensities, and specific regional conditions. It can study
56 how these environmental factors individually and interactively affect soil properties, enhancing understanding of variability
57 and causality (Fontúrbel et al., 2012). Despite the significant spatial and temporal variability in data on site, laboratory
58 burning tests can more accurately analyze the impact of fires on soil by controlling variables, thus minimizing the
59 interference of geographical variations in research outcomes. Such laboratory simulations replicate natural bushfire
60 mechanisms, offering an alternative analytical technique (Pereira et al., 2019). Therefore, laboratory burning tests are
61 recognized for their significant advantages in safety, controllability, reproducibility, and validity when determining changes
62 in soil properties before and after bushfires compared to investigations conducted on site.



63 Assessing post-fire landslides requires studying changes in the force balance of slope soils. Landslides occur when shear
64 stress exceeds the shear strength of slope materials (Sidle and Ochiai, 2006). Previous research on post-fire slope stability
65 has primarily focused on erosion or debris flow initiation using historical data, empirical studies, or statistical models. Staley
66 et al. (2017) defined new logistic regression equations for predicting debris-flow likelihood from empirical databases and
67 refined geospatial analysis. Gartner et al. (2008) developed an empirical model to estimate debris-flow volumes across
68 diverse regions and geological contexts. Compared to these statistical approaches, limited studies have directly used methods
69 based on the formation mechanisms of post-fire slope failures. Few studies on shallow landslides after bushfires have
70 identified the primary triggering mechanism as the loss of structural support from roots (Akin et al., 2023). This loss results
71 in decreased soil shear strength and increased pore water pressure following wetting events due to rising groundwater levels,
72 which are highly correlated to landslide occurrence after bushfires. Furthermore, landslides can occur immediately after the
73 first rainy season following a fire or months to years later (Cannon and Gartner, 2005; Meyer et al., 2001; May and
74 Gresswell, 2003). To establish changes in slope stability before and after fires, it is necessary to differentiate the effects of
75 the fire from triggering meteorological conditions, such as rainfall.

76

77 Understanding post-fire slope stability during rainfall is crucial for mitigating hazards. The Wye River-Jamieson Track
78 Bushfire, which began on 19 December 2015, caused severe eucalyptus vegetation loss in the townships of Wye River and
79 Separation Creek along the Great Ocean Road in the Otway Ranges, Australia. Ten months after the bushfire, heavy rain
80 caused landslides that temporarily closed the road, impeding recovery efforts (Colls and Miner, 2021). This study is based on
81 rainfall data and slope failures that occurred during this period. The loss of vegetation, reduced soil shear strength, and
82 increased pore water pressure are considered key factors for the mechanism of landslide occurrences in burned slopes. This
83 study aims to assess changes in slope stability during rainfall before and after the fire. For this purpose, soil samples were
84 taken from unburned locations near the burned area, and controlled laboratory burning tests were conducted to simulate
85 bushfire effects on soils. Measurements of soil texture, infiltration capacity, and shear strength were performed before and
86 after burning, with pairwise comparisons. Using a simplified hydrological approach-based numerical method (Wakai et al.,
87 2019; Ozaki et al., 2021; Nguyen et al., 2022), this study assessed slope stability during rainfall by comparing groundwater
88 level depth, surface water depth, and safety factor before and after the bushfire. The findings contribute to understanding
89 landslide-triggering mechanisms in post-fire slopes and provide insights for land management and disaster prevention in fire-
90 prone regions.

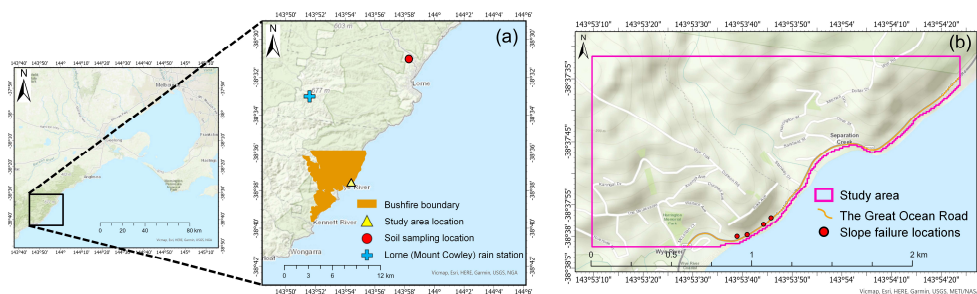
91 **2 Scope of the study**

92 **2.1 The 2015 Wye River-Jamieson Track bushfire and subsequent observed slope failures**

93 The 2015 Wye River-Jamieson Track bushfire, ignited by lightning strikes in the Great Otway National Park, 130 km
94 southwest of Melbourne, Australia, erupted on 19 December 2015 (hereafter referred to as the 2015 bushfire). Severe



95 weather caused the fire to breach containment lines on 24 December, impacting Wye River and Separation Creek. The 2015
96 bushfire destroyed 98 houses in Wye River and 18 houses in Separation Creek, prompting emergency alerts. It burned for 34
97 days until containment on 21 January 2016, scorching over 2500 ha (Fig. 1a). Economic losses were estimated at over 60
98 million dollars. The affected regions, covered by flammable eucalyptus forests, experienced record heat in December 2015
99 and below-average rainfall, which increased fuel levels (State Government of Victoria, 2016). Wye River and Separation
100 Creek are located on steep, southeastern slopes surrounded by rugged terrain, posing challenges for firefighting and
101 evacuation. As two adjacent towns, Wye River and Separation Creek are connected by the Great Ocean Road. They lie in the
102 Otway Ranges, one of Australia's most landslide-prone regions, with significant landslide events typically linked to high
103 annual rainfall (Dahlhaus and Miner, 2002). The Paddy's Path landslide was first observed in Wye River and Separation
104 Creek following a daily rainfall of approximately 60 mm on 14 September, the highest recorded in 2016. The Paddy's Path
105 landslide covered an area approximately 30 m wide by 40 m long (Colls and Miner, 2021), leading to the closure of the
106 Great Ocean Road for three weeks and months of traffic restrictions. This study aims to assess slope stability after the 2015
107 bushfire, focusing on slope failures following rain events around 14 September 2016. The study location (latitude: 38°37'31"
108 S, longitude: 143°54'24" E) was determined by comparing aerial photographs from Google Earth before and after the 2015
109 bushfire and subsequent rain events (Fig. 1a). This study area includes major residential areas and roads like Paddy's Path
110 and the Great Ocean Road, where slope failures occurred (Fig. 1b).



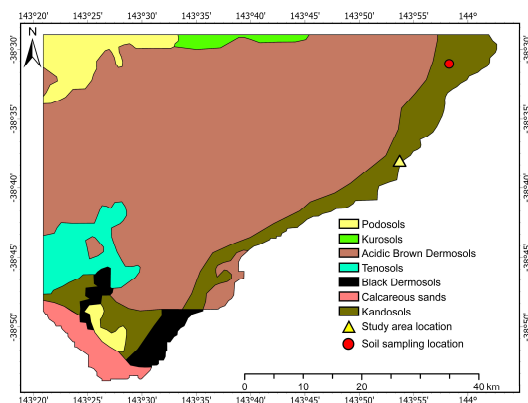
111
112 **Figure 1: (a) Boundary affected by the 2015 bushfire, and locations of the study area and soil sampling (adapted from Colls and**
113 **Miner, 2021). (b) Study area and slope failure locations. (from ESRI)**

114 2.2 Soil sample collection

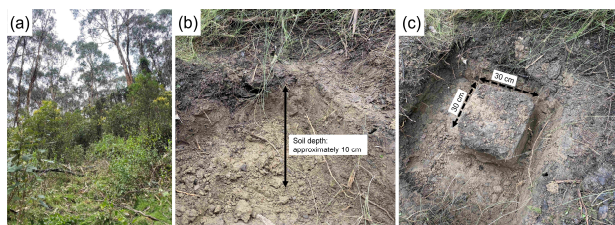
115 Bushfires lead to changes in ground material properties, potentially reducing slope stability. However, the recovery time of
116 soil properties after a bushfire remains unclear (Akin et al., 2023). To compare slope stability before and after the 2015
117 bushfire, soil sampling was conducted in Lorne, an area unaffected by the 2015 bushfire. This sampling location, 16 km
118 from the study area, has similar climatic and rainfall conditions, and the same types of rock and soil (Fig. 2). The sampling
119 location in Lorne shows no signs of vegetation or soil burn (Fig. 3). Both disturbed and undisturbed soil samples were
120 collected: undisturbed samples using cylindrical and block sampling techniques, and disturbed samples from depths



121 exceeding 10 cm below the ground surface. Soil burning tests in laboratory were employed to simulate bushfire impact and
122 understand changes in post-fire soil properties.



123
124 **Figure 2: Soil map of the study area and sampling location (using ESRI adapted from Agriculture Victoria, 2014).**



125
126 **Figure 3: (a) Unburned slope for soil sampling. (b) Soils on site, with disturbed samples taken from soil depths exceeding 10 cm. (c)**
127 **In situ block soil sample (L: 30 cm; W: 30 cm; H: 30 cm).**

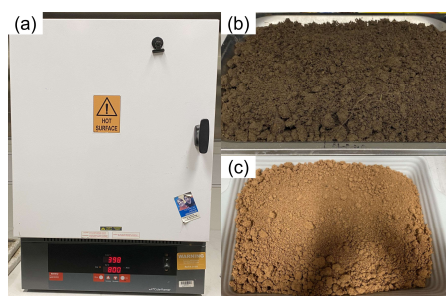
128 3 Laboratory burning test for bushfire simulation

129 3.1 Laboratory burning test conditions

130 Laboratory simulations, often using muffle furnaces, are commonly employed to study bushfire effects on soil properties by
131 imitating the direct impact of temperature on soil (Pereira et al., 2019). This technique has proven effective in simulating
132 bushfire effects (Galang et al., 2010). Peak temperature and duration of burning are the main factors influencing soil
133 changes, necessitating careful control of test conditions (Pereira et al., 2019). However, obtaining retrospective soil
134 temperature data is challenging. Soil temperatures during bushfires typically range from 25 to 900 °C, and high-severity
135 burns reach up to 800 °C, consuming all litter and leaving bare earth (Soto et al., 1991; Mataix-Solera et al., 2011). Peak
136 temperatures as high as 1100 °C have been recorded worldwide (Goudie et al., 1992). Thus, the peak temperature of
137 bushfires is generally thought to be above 800 °C. According to the burn severity map of the 2015 bushfire (Noske et al.,



138 2022), most of the study area, particularly where slope failures were observed, experienced high-severity burning, resulting
 139 in the destruction of all understory vegetation and scorching or burning of the canopy. Consequently, the maximum
 140 temperature for the burning test was set at 800 °C. To prevent soil splashing, the samples were dried in an oven at 100 °C
 141 overnight before placement in the furnace. The dried soil samples reached 800 °C in 1 h. Following the standard procedure
 142 for laboratory burning tests (Giovannini, 1994), the samples were maintained at 800 °C for 30 min. After cooling to the
 143 laboratory temperature around 20 °C, the samples were examined for changes in soil properties. Following these procedures,
 144 laboratory burning tests were conducted on both disturbed and undisturbed soil samples to simulate post-fire soil conditions
 145 (Fig. 4). A series of soil parameters were measured before and after burning, and the effects of the bushfire on soil properties
 146 are described in the following sections and summarized in Table 1.



147
 148 **Figure 4: (a) The furnace. (b) Unburned soil. (c) Burned soil.**

149 **Table 1: Summary of test results.**

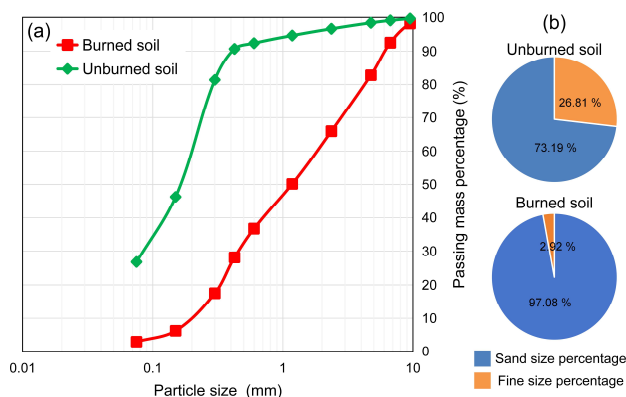
Test results	Soil conditions	
	Unburned	Burned
Moisture content, w (%)	18.93	/
Wet density, ρ_t (g cm^{-3})	1.71	/
Dry density, ρ_d (g cm^{-3})	1.44	1.42
Soil particle density, ρ_s (g cm^{-3})	2.67	2.66
Void ratio, e	0.85	1.20
Liquid limit, w_L (%)	23.19	0
Plastic limit, w_P (%)	18.65	0
Plasticity index, I_p (%)	4.55	0
Hydraulic conductivity, K (m s^{-1})	2.16E-07	9.15E-06
Internal friction angle, ϕ (deg.)	39.33	40.24
Cohesion, c (kN m^{-2})	6.41	0.45



150 3.2 Soil characteristics before and after burning

151 3.2.1 Changes in soil texture

152 Soil texture represents the particle size distribution in the soil. Disturbed soil samples were burned following the procedures
153 in Sect. 3.1 to obtain burned soil. Grain size accumulation curves were generated using particle size distribution tests to
154 illustrate changes in soil texture before and after burning (Fig. 5). According to the Particle Size Classification in the
155 Australian Standard (Standards Australia, 2009), the soil was classified as fine sand (particle size limits: 200 μm to 60 μm)
156 before burning and as coarse sand (particle size limits: 2 mm to 600 μm) after burning. The curves indicate a decrease in fine
157 particle content and an increase in coarse particle content after burning, suggesting soil texture coarsening due to particle
158 bonding from heat. The primary reason for this phenomenon is that clay particles have a lower temperature threshold than
159 sand particles, making them more susceptible to change during fires (Neary et al. 2005).

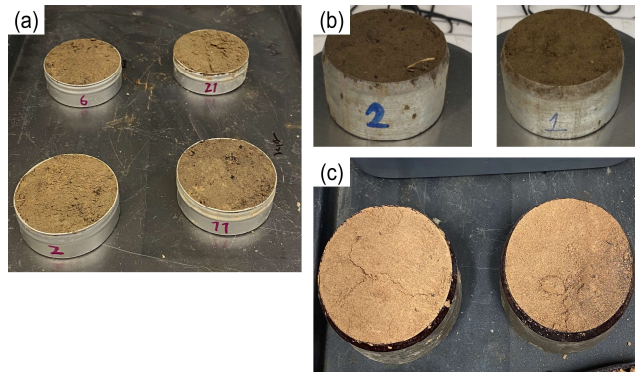


160

161 **Figure 5: (a) Grain size accumulation curve. (b) Particle size percentage for unburned and burned soils.**

162 3.2.2 Changes in physical soil properties

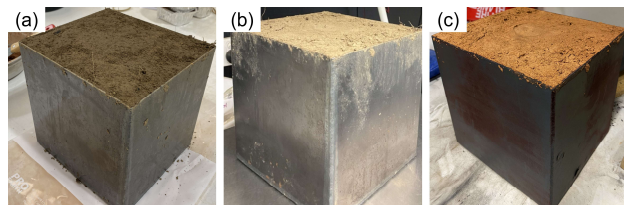
163 Physical properties of soils before and after burning were obtained using disturbed and undisturbed soil samples (Figs. 4 and
164 6), including moisture content, density, void ratio, and soil particle density (Table 1). The void ratio was calculated from dry
165 density and soil particle density. The results for moisture content, dry density, and wet density before burning were obtained
166 from undisturbed soil samples in cylindrical container A (Diameter: 62 mm; Height: 20 mm) shown in Fig. 6a. The value of
167 dry density after burning was determined from undisturbed soil samples in cylindrical container B (Diameter: 82 mm;
168 Height: 42 mm) shown in Fig. 6b-c. Comparison of the results confirms a slight decrease in dry density and soil particle
169 density after burning. This is consistent with the change in soil texture due to increased coarse particles. Therefore, the
170 increase in particle size from burning resulted in a higher void ratio, and reduced plasticity and elasticity of burned soils
171 were demonstrated based on the results of soil consistency limits. Giovannini et al. (1988) reported that high temperatures
172 promote the dispersion of soil aggregates, leading to a loss of stability.



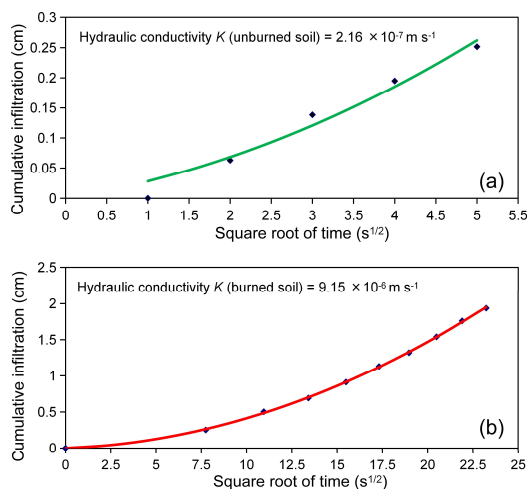
173
174 **Figure 6: (a) Cylinder sample A. (b) Unburned cylinder sample B. (c) Burned cylinder sample B.**

175 3.2.3 Changes in soil hydraulic conductivity- K

176 Soil hydraulic conductivities were measured on undisturbed block soil samples (Fig. 7; L: 20 cm; W: 18 cm; H: 20 cm)
177 before and after burning using the Mini Disk Infiltrometer (manufactured by METER Group, Inc., USA). The results shown
178 in Fig. 8 indicate a significant increase in the permeability of burned soils, due to increased soil porosity caused by larger
179 particle sizes.



180
181 **Figure 7: (a) Wet block soil sample. (b) Dry block soil sample. (c) Burned block soil sample.**

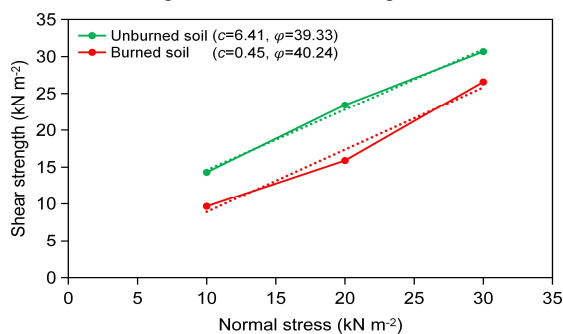


182

183 **Figure 8: Infiltrimeter test results of hydraulic conductivity (a) before and (b) after burning.**

184 3.2.4 Changes in soil mechanical properties- c , φ

185 The results of shear strength parameters, c and φ , were obtained from direct shear tests conducted using disturbed soil
186 samples before and after burning (Fig. 9). Comparison of the results reveals that while the internal friction angle (φ) did not
187 change considerably after burning, the cohesion (c) was significantly reduced. Sect. 3.2.1 demonstrates that burning enlarged
188 soil particles, changing the soil type from fine sand to coarse sand. This disruption of the original soil structure reduced
189 cohesion, resulting in decreased shear strength.



190

191 **Figure 9: Results of direct shear test**



192 4 Numerical method

193 4.1 Profile of the model

194 This study utilized a simplified hydrological method to assess slope stability (Wakai et al., 2019; Ozaki et al., 2021; Nguyen
195 et al., 2022). The method assumes that the slope comprises a shallow impermeable layer (bedrock) overlain by permeable
196 and homogeneous surface soil, allowing it to simulate various rainfall infiltration mechanisms due to differing permeability.
197 Based on particle size distribution test results, the pre-bushfire slope was simulated using the fine sand model, which is
198 characterized by relative low permeability. The post-bushfire slope, with increased permeability, was modelled using the
199 medium-coarse sand model. The method involves four main components: calculating rainfall infiltration, predicting
200 groundwater level fluctuations, modelling surface water, and performing a simple stability calculation using the semi-infinite
201 slope assumption. Subsequent sections provide brief descriptions of these components.

202 4.2 Calculating rainfall infiltration

203 The first step involves calculating rainfall infiltration, separating rainfall into infiltration from the ground surface and surface
204 runoff at each time. Green and Ampt (1911) proposed a simplified equation for one-dimensional vertical rainfall infiltration
205 into a uniform soil profile under surface ponding conditions. This study used the modified Green-Ampt model by Mein and
206 Larson (1973) and Chu (1978) for infiltration analysis, conforming to the homogeneous-slope assumption and the slope
207 angle influence described by Wakai et al. (2019). The modified equation can accommodate changes in rainfall over a short
208 time interval (Δt), as follows:

$$209 \quad f(t + \Delta t) = K_s [1 + \Delta h \Delta \theta / F(t + \Delta t)], \quad (1)$$

$$210 \quad F(t + \Delta t) = F(t) + K_s \Delta t + (\Delta h \Delta \theta) \ln \left(\frac{F(t + \Delta t) + \Delta h \Delta \theta}{F(t) + \Delta h \Delta \theta} \right), \quad (2)$$

$$211 \quad F_p = K_s (\Delta h \Delta \theta) / (R(t) - K_s), \quad (3)$$

212 Where $f(t + \Delta t)$ is infiltration capacity at time $t + \Delta t$; $F(t)$ and $F(t + \Delta t)$ are cumulative infiltration at time t and $t + \Delta t$,
213 respectively; $\Delta \theta$ is change in volumetric water content; K_s is saturated hydraulic conductivity; $R(t)$ is rainfall intensity; F_p is
214 cumulative infiltration at the start of ponding; and $\Delta h = (h + \psi_f)$ is the driving matric pressure head, where h is the surface
215 water depth and ψ_f is the matric suction at the wetting front.

216

217 The infiltration capacity (f) determines the amount of infiltration water (I) at each step. If the total amount of precipitation
218 (R) and surface water (SW) is less than the infiltration capacity (f), all the water will be absorbed into the soil. If the total
219 amount exceeds the infiltration capacity (f), the infiltration water (I) equals the infiltration capacity (f).



$$220 \quad I = \begin{cases} SW + R, & \text{if } (SW + R) \leq f \\ f, & \text{if } (SW + R) > f \end{cases} \quad (4)$$

221 4.3 Predicting fluctuations in groundwater level

222 The second step involves modelling the spatial distribution of groundwater, which includes vertical infiltration from the
223 ground surface and lateral infiltration of groundwater in the saturated zone of the slope. The predictive model in this study
224 assumes that fluctuations in shallow groundwater levels of natural slopes are calculated based on a single geological
225 composition. Materials are categorized as medium-coarse sand and fine sand due to their significantly different infiltration
226 characteristics. This section briefly explains the proposed models for medium-coarse sand and fine sand. The medium-coarse
227 sand model, developed by Nguyen et al. (2022), predicts groundwater rise on natural slopes at a relatively shallow depth. To
228 determine the analytical parameters for this method, parametric studies were conducted using the VGFlow model (Cai and
229 Ugai, 2004), controlling slope conditions such as permeability, slope angle, and initial moisture. The prediction for
230 groundwater level rise is simply assumed to be divided into two periods. In the first period, the degree of saturation increases
231 at a nearly constant rate without a groundwater level rise until the unsaturated area receives more rainwater than its capacity.
232 In the second period, the groundwater level rises at a nearly constant rate. The modelling of the vertical infiltration process
233 focuses on these two periods. The elapsed time (t_1) before the groundwater level begins to rise is determined as follows.

$$234 \quad t_1 = \frac{h}{I} \left(\theta_{cp} - n \frac{S_{r0}}{100} \right), \quad (5)$$

235 Where I is infiltration water; n is soil porosity; h is the initial thickness of the unsaturated layer; S_{r0} is the initial degree of
236 saturation at the start of rainfall; and θ_{cp} is the limit of the mean volumetric water content in the unsaturated layer before the
237 groundwater table starts to rise.

238

239 The rise velocity of the groundwater level (v_{wl}) after it starts rising steadily is defined by the theoretically required amount
240 of water to saturate the pores in the unsaturated layer, with an adjustment parameter α_v to match results (Wakai et al., 2019).
241 Assuming the critical degree of saturation corresponding to the start of groundwater level rise is S_r^* , the elapsed time (t_2)
242 before the groundwater level reaches the ground surface is defined by the following equation.

$$243 \quad t_2 = \frac{h}{v_{wl}} = \frac{n \left(1 - \frac{S_r^*}{100} \right) h}{\alpha_v I}, \quad (6)$$

244 Equations (5) and (6) are applied to calculate changes in groundwater level due to vertical infiltration during rainfall events.
245 A planar flow analysis model for shallow groundwater is essential when lateral groundwater inflow/outflow affects slope
246 stability. The governing equation for the seepage field, considering only lateral seepage flow in the unconfined aquifer, is
247 defined by Eq. (7) (Japanese Association of Groundwater Hydrology, 2010).



$$248 \quad \frac{\partial}{\partial x} \left(T_{xx} \frac{\partial \Phi}{\partial x} \right) + \frac{\partial}{\partial y} \left(T_{yy} \frac{\partial \Phi}{\partial y} \right) = n_e \frac{\partial \Phi}{\partial t}, \quad (7)$$

249 Where T_{xx} and T_{yy} are transmissivities in the x- and y-axis directions in planar coordinate systems, respectively; n_e is
250 effective porosity; and Φ is the total head of groundwater. The explicit method proposed by Kinzelbach (1986) can be
251 employed to differentiate the equation.

252

253 In the medium-coarse sand model, the saturation process moves upward from the bedrock to the surface. Different from the
254 medium-coarse sand model, which predicts groundwater level rise during rainfall, the fine sand model proposed by Ozaki et
255 al. (2021) focuses on simulating the downward movement of the high-saturation zone (wetting front) from the ground
256 surface. Ozaki et al. (2021) theoretically determined the downward velocity (v_{bs}) of the wetting front based on the water
257 required to saturate the pores in the unsaturated layer. However, in practical applications, slightly different values can be
258 obtained depending on conditions. The fine sand model uses Eq. (8) to calculate the downward velocity, multiplied by the
259 correction factor (β_v) for generalization.

$$260 \quad v_{bs} = \frac{\beta_v I}{n \left(1 - \frac{S_{r0}}{100} \right)}, \quad (8)$$

261 Where n is soil porosity; S_{r0} is the initial degree of saturation at the start of rainfall; and I is a constant rainfall intensity.

262

263 The elapsed time (t_3) from the start of rainfall until all the unsaturated layers (vertical thickness: h) below the groundwater
264 level reach saturation and the infiltration front reaches the initial groundwater level can be calculated using Eq. (9). If there is
265 no groundwater level, the infiltration front reaches the undrained edge at the bottom of the analysis area. The fine sand
266 model focuses solely on the vertical rainwater infiltration component and does not account for the horizontal component.

$$267 \quad t_3 = \frac{h}{v_{bs}} = \frac{n \left(1 - \frac{S_{r0}}{100} \right) h}{\beta_v I}, \quad (9)$$

268 4.4 Modelling surface water

269 The surface water model uses the shallow-water equations, derived from the equations of conservation of mass and linear
270 momentum (Navier–Stokes equations) (Di Giammarco et al., 1996).

271 Law of conservation of mass:

$$272 \quad \frac{\partial h}{\partial t} + \frac{\partial(hu)}{\partial x} + \frac{\partial(hv)}{\partial y} = i \quad (10)$$

273 The Navier–Stokes equations:

$$274 \quad \frac{\partial(uh)}{\partial t} + \frac{\partial(hu^2)}{\partial x} + \frac{\partial(huv)}{\partial y} + gh(S_{fx} + \frac{\partial H}{\partial x}) = 0, \quad (11)$$



$$275 \quad \frac{\partial(vh)}{\partial t} + \frac{\partial(hu)}{\partial x} + \frac{\partial(hv^2)}{\partial y} + gh \left(S_{fy} + \frac{\partial H}{\partial y} \right) = 0, \quad (12)$$

276 Where $H(x, y, t)$ is water surface elevation above a horizontal datum; $h(x, y, t)$ is local water depth; t is time; x and y are
277 horizontal coordinates; $u(x, y, t)$ and $v(x, y, t)$ are flow velocities in x and y directions; $i(x, y, t)$ is net input rainfall;
278 $S_{fx}(x, y, t)$ and $S_{fy}(x, y, t)$ are friction slopes in the x and y directions; and g is gravitational acceleration.

279

280 To simplify the complex equations, the insignificant influence components are removed (Di Giammarco et al., 1996; Zhu et
281 al., 2020). They are replaced by the diffusion wave approximation equations, written as Eqs. (13) and (14).

$$282 \quad S_{fx} + \frac{\partial H}{\partial x} = 0, \quad (13)$$

$$283 \quad S_{fy} + \frac{\partial H}{\partial y} = 0, \quad (14)$$

284 These equations are solved using the finite-difference technique in the MIKE SHE model (DHI, 2007). The change in water
285 depth from time step t to $t + \Delta t$ can be calculated as:

$$286 \quad \Delta h = h(t + \Delta t) - h(t) = i \cdot \Delta t + \frac{\sum Q \Delta t}{\Delta x^2}, \quad (15)$$

287 Where $\sum Q$ represents the total flow volume from four directions at the calculated node. The discharge from an upstream
288 node to a downstream neighbor is approximately calculated in Eq. (16):

$$289 \quad Q = \frac{K \Delta x}{\Delta x^2} (H_U - H_D)^{1/2} h_u^{5/3}, \quad (16)$$

290 Where (H_D, h_D) and (H_U, h_U) are the sets of the local water level and water depth of the downstream and upstream nodes,
291 respectively; h_u is the free water depth of the upstream node that can flow into the downstream neighbor; and K is the
292 Strickler coefficient, calculated as the inverse of the Manning coefficient, reflecting the roughness of the ground surface in
293 the calculation.

294 4.5 Performing simple stability calculation using the semi-infinite slope assumption

295 When soil thickness is considerably smaller than slope length, an infinite plane slope can suitably approximate a hillslope
296 (Montgomery and Dietrich, 1994). This study uses the Mohr-Coulomb failure law to assess slope stability, considering shear
297 strength (soil resistance to shearing) and shear stress (downslope component of soil weight) along the potential failure plane.
298 The safety factor (F_s) is the ratio of shear strength to shear stress. The sliding surface is assumed planar, infinitely extended,
299 and coinciding with the interface between the soil cover layer and the impermeable layer. Slope stability is considered
300 unstable when F_s is less than 1.0. Differences in the definitions of F_s between medium-coarse sand (Eq. 17) and fine sand
301 (Eq. 18) arise from the consideration of water pressure on the sliding surface, based on the semi-infinite slope assumption.



302 For the medium-coarse sand model:

$$303 \quad F_s = \frac{\tau_f}{\tau} = \frac{c' + [\gamma_t \cdot h_1 + (\gamma_{sat} - \gamma_w) h_2] \cos^2 \theta \cdot \tan \phi'}{(\gamma_t \cdot h_1 + \gamma_{sat} \cdot h_2) \sin \theta \cdot \cos \theta}, \quad (17)$$

304 For the fine sand model:

$$305 \quad F_s = \frac{\tau_f}{\tau} = \frac{c' + \gamma_{sat} \cdot H \cdot \cos^2 \theta \cdot \tan \phi'}{\gamma_{sat} \cdot H \cdot \sin \theta \cdot \cos \theta} \quad (18)$$

306 Where τ is the shear stress due to the sliding direction component of gravity of soil; τ_f is the shear strength of soil, which is
307 the maximum shear resistance; γ_t is the wet unit weight of soil; γ_{sat} is the saturated unit weight of soil; γ_w is the unit weight
308 of water; h_1 is the depth from the ground surface to the groundwater level; h_2 is the depth from the groundwater level to the
309 slip surface, which may correspond to the surface of the base layer; H is the depth from the ground surface to the wetting
310 front; θ is the slope inclination angle; c' is the cohesion of soil; and ϕ' is the angle of shear resistance of soil.

311 5 Slope stability analysis before and after the 2015 bushfire

312 5.1 Failure mechanisms of post-fire slope

313 Based on the results of burning tests in Sect. 3, bushfires significantly affect soil properties, causing hazards such as hillslope
314 runoff, debris flows, and shallow landslides (Culler et al., 2023). A key effect is changes in soil water repellency, referring to
315 the inability of water to wet or infiltrate dry soil. This repellency may be strengthened or diminished depending on the
316 timescales post-fire (Varela et al., 2015). During the initial post-fire period, increased water repellency can occur a few
317 centimeters below the surface due to the formation of an impermeable layer from ash particles clogging soil micropores
318 (Mallik et al., 1984). However, soil water repellency changes over time. Strong winds can clear bushfire ash within days, and
319 rainfall can wash away the hydrophobic layer, increasing infiltration capacity (Pereira et al., 2013; Liu et al., 2021). Another
320 significant impact is the loss of root reinforcement. The losses lead to a decrease in shear strength by 55 %-82 % in the
321 months or years following a fire, and this decrease persists depending on fire severity, plant resistance, and regeneration rate
322 (Lei et al., 2022). It has been found that soil infiltration capacity can recover about a year after a fire, but the effects of root
323 loss continue to dominate, reducing tensile strength, hydrophobicity, and shear strength (Lanini et al., 2009).

324

325 Considering the post-fire timescales, failure mechanisms during heavy rainfall events can be categorized into two patterns.
326 The first pattern occurs shortly after a fire when soil water repellency is dominant. Vegetation losses and changes in soil
327 texture increase infiltration capacity, but ash from burned vegetation can block soil pores, forming a sealing layer. This layer
328 causes rainwater to accumulate, resulting in runoff and erosion. The second pattern, occurring after a longer period, is due to
329 decreased soil strength from reduced root systems. Reduced roots decrease transpiration and soil suction, lowering shear
330 strength (Ng and Menzies, 2014). Rising groundwater levels after rainfall elevate pore pressure, triggering slope failures or



331 large-scale landslides. This mechanism is related to root cohesion, with the depth and concentration of fire-damaged roots
332 influencing the sliding surface position. This study focuses on a post-fire timescale of approximately ten months, aligning
333 with the second pattern of failure mechanism, where root reduction predominates, leading to decreased soil shear strength.

334 5.2 Study area and data used for analysis

335 According to the Köppen-Geiger classification, the study area has a maritime temperate climate with warm summers and
336 cool winters, and 60 %-65 % of the annual rainfall occurring from May to October (Linforth, 1977). The vegetation in the
337 study area is classified as eucalypt open forest, a key resource for the timber industry (Specht, 1970). Approximately 48 % of
338 fires larger than 1000 ha from 2006 to 2016 occurred in eucalypt open forests. The geology of the study area is identified as
339 the Early Cretaceous Eumeralla Formation, Otway Group, dominated by sandstone lithology (Edwards et al., 1996). This
340 geological unit is known for its high landslide susceptibility in southwestern Victoria due to rapid weathering. The soil type
341 is classified as Kandosols, mainly found in areas underlain by Cretaceous sediments (Isbell, 2016). Kandosols, which lack
342 strong texture contrast between surface and subsoil horizons and often have weak or no structure, good drainage, and
343 permeability, are prone to sliding on steep slopes (WGCMA, 2008). The surrounding topography of the study area is steep,
344 featuring highly dissected bedrock knolls and ridges. Fig. 10 shows the distribution maps of elevation and slope for the study
345 area, respectively. Soil depth significantly influences the mechanism of shallow slope failures. In this study, soil depth
346 distribution (y_i) is calculated based on Eq. (19) proposed by Saulnier et al. (1997), which shows an inverse correlation
347 between soil thickness and slope angle.

$$348 y_i = y_{max} \left[1 - \frac{\tan(x_i) - \tan(x_{min})}{\tan(x_{max}) - \tan(x_{min})} (1 - \alpha) \right], \quad (19)$$

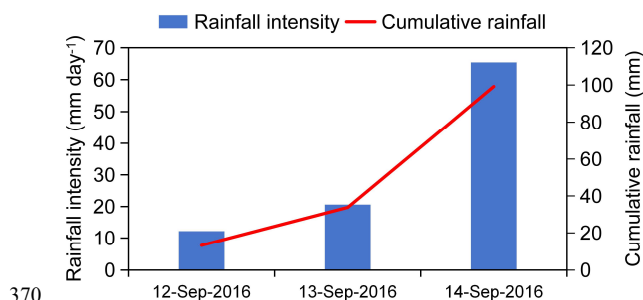
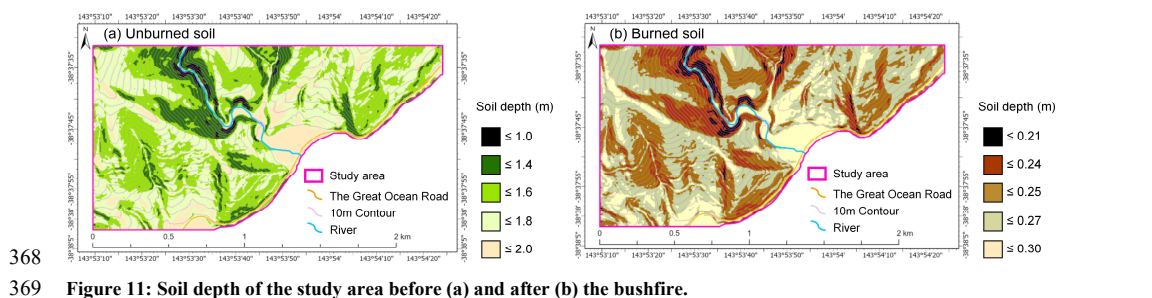
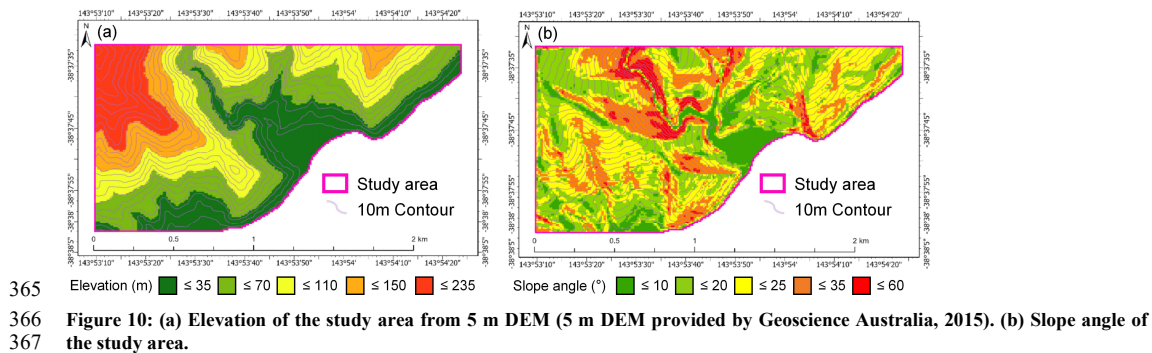
349 Where $\alpha = y_{min}/y_{max}$; y_{min} and y_{max} are the minimum and maximum values of effective soil depth, respectively; x_i is the
350 slope angle at element i ; and x_{max} and x_{min} are the minimum and maximum values of slope angle, respectively.

351

352 In this study, the soil depth settings for calculations differ before and after the 2015 bushfire. Based on the soil depth map of
353 Australia (Rossel et al., 2014), the pre-fire minimum and maximum soil depths were set at 0.1 m and 2.0 m, respectively.
354 According to the second failure mechanism outlined in Sect. 5.1, the death and decay of tree roots after the fire reduce shear
355 strength, and the depth and concentration of fire-damaged roots influence the sliding surface position. Since the maximum
356 root concentration is at 0.3 m, significantly impacting soil shear strength (Baldwin and Stewart, 1987), the post-fire
357 minimum and maximum soil depths were adjusted to 0.1 m and 0.3 m, respectively. Fig. 11 shows the distribution maps of
358 soil depth for analysis before and after the bushfire in the study area. Soil parameters for analysis before and after the fire are
359 detailed in Table 2, based on the test results in Sect. 3 and adopted from the study by Rawls et al. (1983). Rainfall data were
360 sourced from the Lorne (Mount Cowley) station, published by BoM, located 12 km from the study area, covering the 72-
361 hour period from 12 to 14 September 2016 (Fig. 11). The 24-hour cumulative rainfall on 14 September was approximately



362 65 mm, consistent with the date and amount of rainfall observed during the post-bushfire landslides recorded by Colls and
 363 Miner (2021). Due to the lack of detailed groundwater level information before the rainfall, the initial groundwater level is
 364 assumed to be at the bottom of the soil depth.





372 **Table 2: Material parameters for analysis.**

Material parameters	Soil conditions	
	Unburned	Burned
Initial saturation degree, S_{r0} (%)	59.45	42.18
Hydraulic conductivity, K (m h ⁻¹)	7.78E-04	3.29E-02
Saturated unit weight, γ_{sat} (kN m ⁻³)	19.0	17.6
Wet unit weight, γ_t (kN m ⁻³)	17.1	14.2
Cohesion, c' (kN m ⁻²)	6.41	0.45
Internal friction angle, ϕ' (deg.)	39.33	40.24

373 **5.3 Results and discussion**

374 The slope stability analysis before the 2015 bushfire used the fine sand model, and the post-fire analysis employed the
 375 coarse-medium sand model. As described in Sect. 4.3, unburned soil with low permeability exhibits a saturated layer from
 376 the surface to the bedrock while burned soil with relatively high permeability shows the groundwater level rising from the
 377 bedrock to the surface. Fig. 13a displays the maps of the wetting front depth from the ground surface before the fire from 12
 378 to 14 September 2016. Fig. 13b shows the maps of the groundwater level depth after the fire, referring to the distance from
 379 the ground surface to the groundwater level. Before the fire, at 00:00 on 12 September, no obvious distributions of wetting
 380 front depth are observed in the study area. The distributions of wetting front depth begin to change significantly at 00:00 on
 381 13 September and gradually become deeper with increasing rainfall. By the end of heavy rainfall at 00:00 on 15 September,
 382 the wetting front depth reaches the bedrock surface in almost all slopes. After the fire, the groundwater level reaches the
 383 ground surface in some slopes of the study area at 00:00 on 13 September and rises significantly with increasing cumulative
 384 rainfall, reaching the ground surface in almost all slopes by 00:00 on 15 September. Due to the thinner maximum depth of
 385 fire impact on surface soil (0.3 m post-fire vs. 2.0 m pre-fire), the post-fire groundwater level reaches the ground surface
 386 earlier.

387

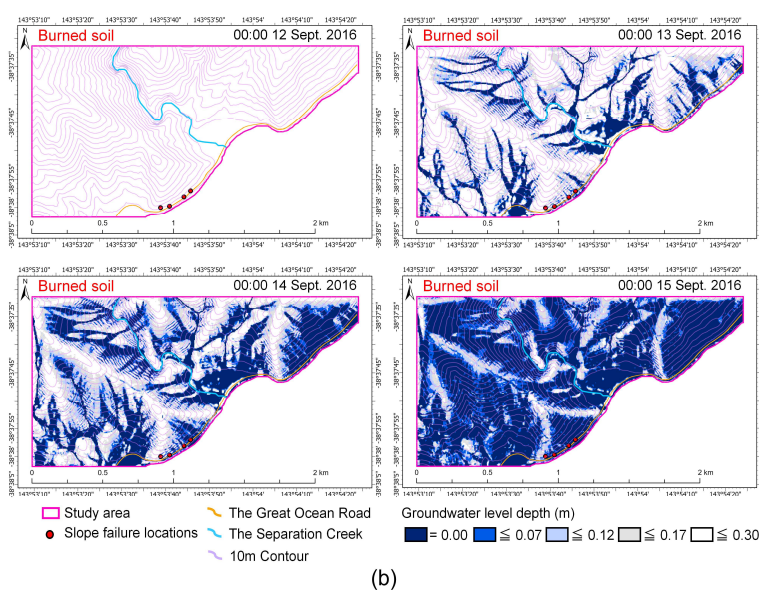
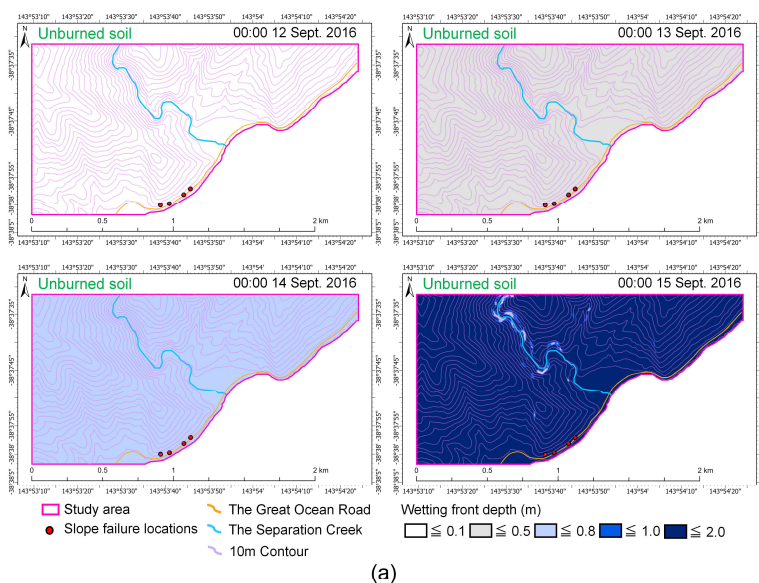
388 Figure 14 shows maps of surface water level depth from the ground surface before and after the fire, from 12 to 14
 389 September 2016. Before the fire, surface water first appears near Separation Creek around 00:00 on 14 September, consistent
 390 with the wetting front depth trend at the same time point (Fig. 13a). A larger area of surface water forms at 00:00 on 15
 391 September. After the fire, some slopes show the groundwater level reaching the ground surface at 00:00 on 13 September,
 392 making rainwater infiltration difficult and leading to surface water formation. Surface water tends to concentrate in valleys
 393 and widen over time, appearing in almost the entire study area by 00:00 on 15 September. The areas of surface water
 394 generally align with higher groundwater levels. Compared to pre-fire maps, post-fire surface water is distributed over a
 395 larger extent and in more areas of high-level surface water.



396 The calculation formulas for the safety factor vary due to different infiltration behaviors (Eqs. 17 and 18). Figure 15 shows
397 the safety factor maps before and after the fire, from 12 to 14 September 2016. Before the fire, the values of safety factor (F_s)
398 decrease with increasing cumulative rainfall but remain above 1 due to the higher shear strength of the pre-fire surface soil,
399 indicating overall stability during the rainfall period. After the fire, from 00:00 on 13 September, the values of F_s sharply
400 drop below 1 throughout the study area. By 00:00 on 15 September, the extent of F_s below 1 significantly expands,
401 indicating potential slope failures, especially in steep slopes and river valleys. Figure 16 shows the magnified maps of F_s
402 before and after the fire at 00:00 on 15 September, respectively. According to Colls and Miner (2021), slope failures,
403 including the Paddy's Path landslide, occurred near the Great Ocean Road in the study area during heavy rainfall on 14
404 September. The results show that the values of F_s of this road segment are above 1 before the fire but drop below 1 after the
405 fire, consistent with the locations of observed slope failures. Thus, the results are considered reasonably reliable and provide
406 a reference for predicting slope hazards in this area.

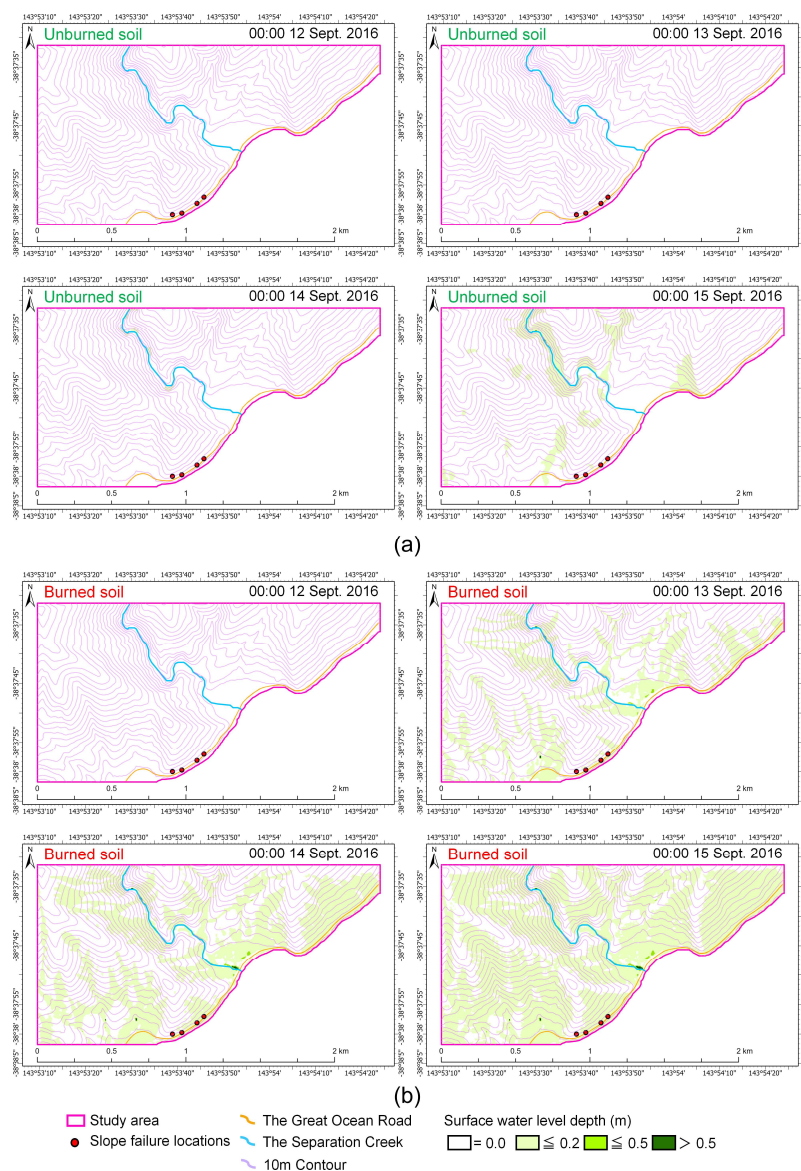
407

408 In some locations of this study area, especially near Separation Creek, the values of F_s are less than 1, indicating instability,
409 however, no slope failures were observed. The lack of a detailed database on slope disasters complicates the identification of
410 slope failures in this study. Spittler and Wagner (1998) reported that regions susceptible to landslides often experience more
411 occurrences following bushfires. According to the landslide susceptibility map of Colac Otway Shire (AS Miner
412 Geotechnical, 2006), the segment of the Great Ocean Road where Paddy's Path landslide occurred is at the highest level of
413 susceptibility, and areas near Separation Creek have a moderate-high level of susceptibility. Thus this segment is considered
414 relatively high-susceptible to landslides after the fire, consistent with the results of safety factor maps. Differences in pre-fire
415 vegetation density also influence soil strength changes and recovery time. Goudie et al. (1992) noted that the highest bushfire
416 temperatures are often in densely vegetated areas. According to the burn severity map of the 2015 bushfire (Noske et al.,
417 2022), the area near the Great Ocean Road had high burn severity with majority crown burn, while the area near Separation
418 Creek had medium burn severity with majority crown scorch, understory burn, and some crown burn. For slope stability
419 calculations, the entire study area was simplified to high burn severity, which may have led to lower assessments of safety
420 factors near Separation Creek after the fire. However, Wondzell and King (2003) suggested that fires can accelerate
421 streambank erosion, potentially increasing slope failures. Thus, special attention should be given to potentially unstable
422 slopes near Separation Creek, and over-assessment of safety factors is reasonable for developing mitigation and prevention
423 strategies.



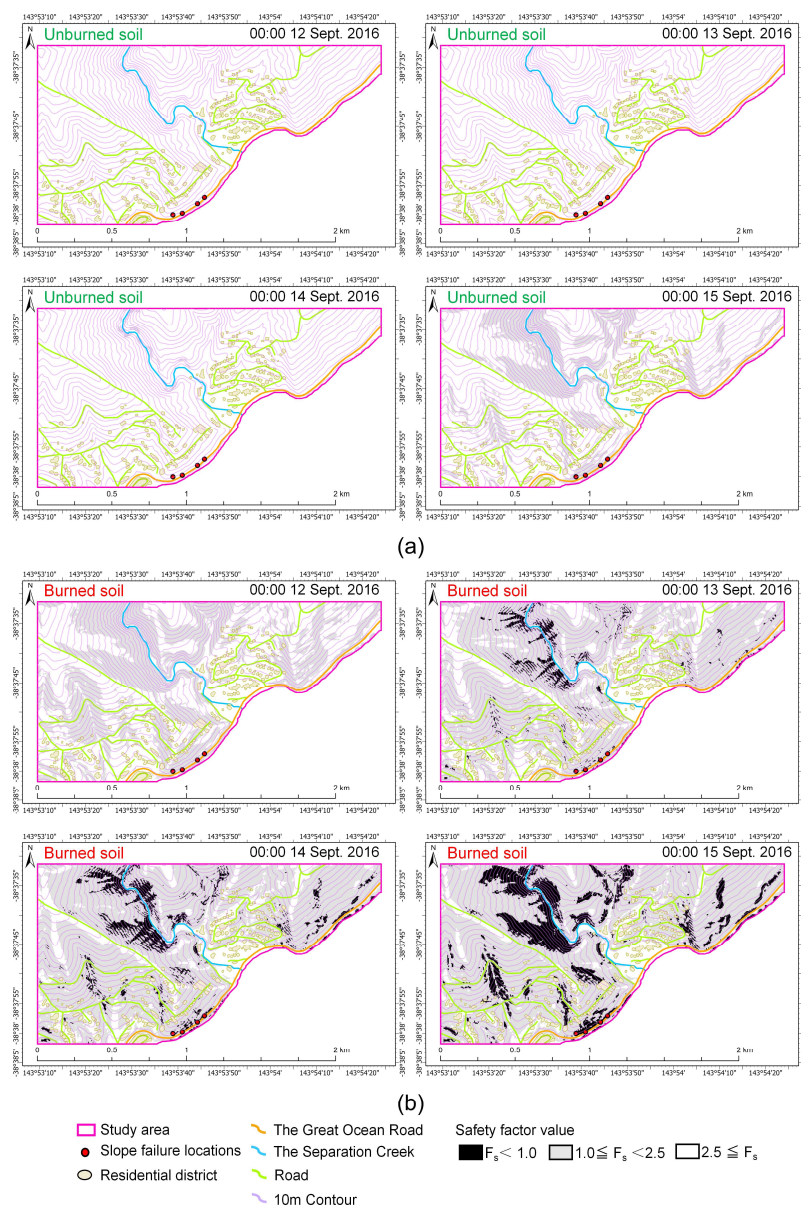
424

425 **Figure 13: (a) Maps of wetting front depth from ground surface pre-bushfire. (b) Maps of groundwater level depth from ground**
 426 **surface post-bushfire.**



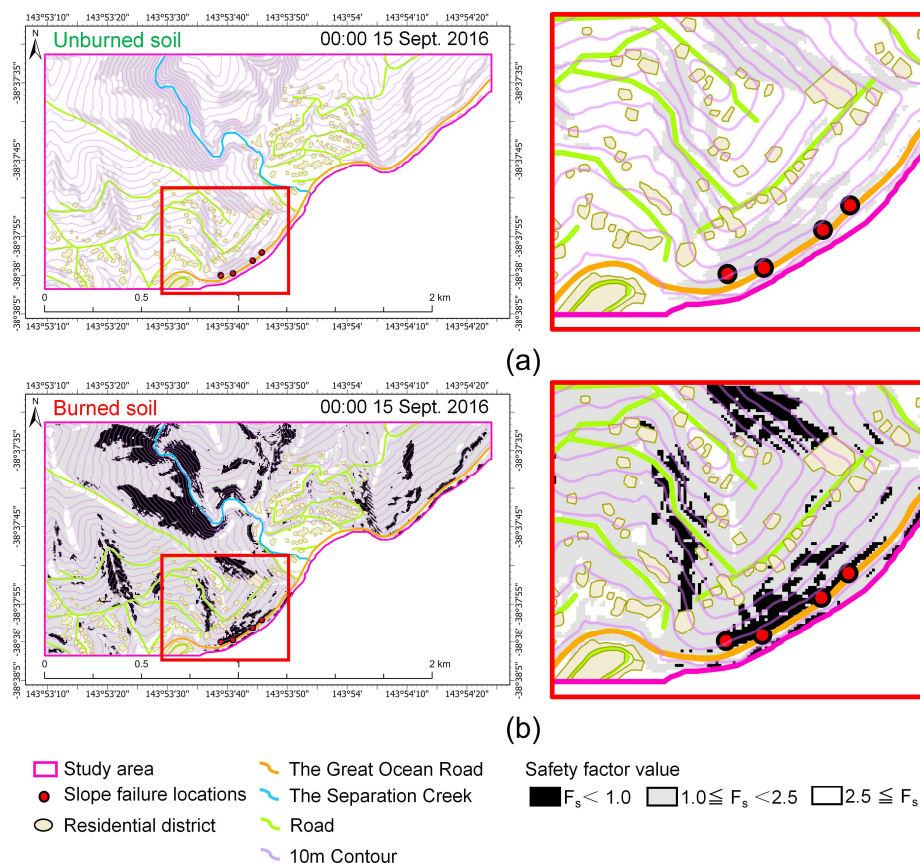
427

428 **Figure 14: Maps of surface water level depth from ground (a) pre-bushfire and (b) post-bushfire.**



429

430 **Figure 15: Maps of safety factor (a) pre-bushfire and (b) post-bushfire.**



431

432 **Figure 16: Magnified maps of safety factor (a) pre-bushfire and (b) post-bushfire.**

433 **6 Conclusions**

434 This study focused on Wye River and Separation Creek in Australia, which were affected by the 2015 Wye River-Jamieson
 435 Track bushfire. Ten months after the bushfire, multiple slope failures were observed during heavy rains from 12 to 14
 436 September 2016, including the Paddy's Path landslide, which disrupted the main road connecting the towns. This indicated a
 437 strong correlation between increased slope hazards and bushfire effects on soils. To determine this correlation, controlled
 438 laboratory burning tests were conducted to simulate the effects of bushfires on soil. The test results showed changes in the
 439 structural, hydrological, and mechanical properties of post-fire soil: coarser soil particles, increased permeability, and
 440 reduced soil shear strength, particularly cohesion. To compare changes in slope stability before and after the bushfire, using



441 a simplified hydrologic numerical model, slope stability assessments during rainfall were performed based on soil
442 parameters before and after the burning tests. The results confirmed significant differences in the time-dependent changes in
443 groundwater level depth, surface water depth, and safety factor during rainfall before and after the bushfire. Before the
444 bushfire, the values of the safety factor decreased with increasing cumulative rainfall but remained above 1, indicating stable
445 slopes in the study area. After the bushfire, due to weakened cohesion, it was observed that as the rainfall-induced
446 groundwater level rose, the values of safety factor fell below 1 in some slopes of the study area, indicating high susceptibility
447 to shallow slope failures. The results of the safety factor were below 1 at the locations where slope failures were observed,
448 confirming the accuracy of this study in capturing disaster occurrences. This study suggested that the dominant failure
449 mechanism of slopes is the reduction in shear strength due to the diminished root system after a bushfire, highlighting the
450 need for effective land management and disaster prevention measures. This information is valuable for future hazard
451 assessments and mapping landslide susceptibility after bushfires.

452 **Code and data availability**

453 Relevant code and data will be available to researchers upon request.

454 **Author contribution**

455 YL, AW, and SC conceptualized this study. YL conducted the experiments and carried out the analysis under the supervision
456 of AW and SC. YL prepared the manuscript draft, which was subsequently reviewed and edited by all co-authors.

457 **Competing interests**

458 The contact author has declared that none of the authors has any competing interests.

459 **Disclaimer**

460 Publisher's note: Copernicus Publications remains neutral with regard to jurisdictional claims made in the text, published
461 maps, institutional affiliations, or any other geographical representation in this paper. While Copernicus Publications makes
462 every effort to include appropriate place names, the final responsibility lies with the authors.



463 **Acknowledgements**

464 The authors are grateful to the Geoscience Australia for providing the DEM data and the Bureau of Meteorology for
465 providing rainfall data. The authors also appreciate the support of Ms. Saya Okabe, Mr. Kosuke Suto, and Ms. Mithushi
466 Wickramasinghe.

467 **References**

- 468 Abdollahi, M., Vahedifard, F., and Tracy, F. T.: Post-Wildfire Stability of Unsaturated Hillslopes Against Rainfall-Triggered
469 Landslides, *Earth Future.*, 11, e2022EF003213, <https://doi.org/10.1029/2022EF003213>, 2023.
- 470 Agbeshie, A. A., Abugre, S., Atta-Darkwa, T., and Awuah, R.: A review of the effects of forest fire on soil properties, *J. For.*
471 *Res.*, 33, 1419–1441, <https://doi.org/10.1007/s11676-022-01475-4>, 2022.
- 472 Agriculture Victoria: https://vro.agriculture.vic.gov.au/dpi/vro/vrosite.nsf/pages/victorian_soils_map_2014, last access: 9
473 October 2020, 2014.
- 474 Akin, I. D., Akinleye, T. O., and Robichaud, P. R.: Changes in Soil Properties over Time after a Wildfire and Implications to
475 Slope Stability, *J. Geotech. Geoenviron. Eng.*, 149, 04023045, <https://doi.org/10.1061/JGGEFK.GTENG-11348>, 2023.
- 476 AS Miner Geotechnical: Landslide and Erosion Susceptibility Mapping in the CCMA Region, University of Ballarat, Report
477 No 306/01/06, 2006.
- 478 Ashe, B., McAneney, K. J., and Pitman, A. J.: Total cost of fire in Australia, *J. Risk Res.*, 12, 121–136,
479 <https://doi.org/10.1080/13669870802648528>, 2009.
- 480 Babrauskas, V. and Grayson, S. J. (Eds.): Heat release in fires, Taylor & Francis, 660 pp., ISBN 0419161007, 1990.
- 481 Badía, D. and Martí, C.: Plant Ash and Heat Intensity Effects on Chemical and Physical Properties of Two Contrasting Soils,
482 *Arid Land Res. Manag.*, 17, 23–41, <https://doi.org/10.1080/15324980301595>, 2003.
- 483 Baldwin, P. J. and Stewart, H. T. L.: Distribution, length and weight of roots in young plantations of *Eucalyptus grandis* W.
484 Hill ex Maiden irrigated with recycled water, *Plant Soil.*, 97, 243–252, <https://doi.org/10.1007/BF02374947>, 1987.
- 485 Bordoloi, S. and Ng, C. W. W.: The effects of vegetation traits and their stability functions in bio-engineered slopes: A
486 perspective review, *Eng. Geol.*, 275, 105742, <https://doi.org/10.1016/j.enggeo.2020.105742>, 2020.
- 487 Bowman, D. M. J. S., Kolden, C. A., Abatzoglou, J. T., Johnston, F. H., van der Werf, G. R., and Flannigan, M.: Vegetation
488 fires in the Anthropocene, *Nat Rev Earth Environ.*, 1, 500–515, <https://doi.org/10.1038/s43017-020-0085-3>, 2020.
- 489 Brucker, C. P., Livneh, B., Minear, J. T., and Rosario-Ortiz, F. L.: A review of simulation experiment techniques used to
490 analyze wildfire effects on water quality and supply, *Environ. Sci.-Process Impacts.*, 24, 1110–1132,
491 <https://doi.org/10.1039/D2EM00045H>, 2022.
- 492 Cai, F. and Ugai, K.: Numerical Analysis of Rainfall Effects on Slope Stability, *Int. J. Geomech.*, 4, 69–78,
493 [https://doi.org/10.1061/\(ASCE\)1532-3641\(2004\)4:2\(69\)](https://doi.org/10.1061/(ASCE)1532-3641(2004)4:2(69)), 2004.



- 494 Cannon, S. H. and Gartner, J. E.: Wildfire-related debris flow from a hazards perspective, in: Debris-flow Hazards and
495 Related Phenomena, edited by: Jakob, M. and Hungr, O., Springer, Berlin, Heidelberg, 363–385, https://doi.org/10.1007/3-540-27129-5_15, 2005.
- 497 Certini, G.: Effects of fire on properties of forest soils: a review, *Oecologia*, 143, 1–10, <https://doi.org/10.1007/s00442-004-1788-8>, 2005.
- 499 Chu, S. T.: Infiltration during an unsteady rain, *Water Resour. Res.*, 14, 461–466,
500 <https://doi.org/10.1029/WR014i003p00461>, 1978.
- 501 Colls, S. and Miner, A. S.: Bushfires, landslides and geotechnical challenges in the Otway Ranges, Victoria, in: NZGS
502 SYMPOSIUM 2021, Dunedin, New Zealand, 24-26 March 2021, 2021.
- 503 Culler, E. S., Livneh, B., Rajagopalan, B., and Tiampo, K. F.: A data-driven evaluation of post-fire landslide susceptibility,
504 *Nat. Hazards Earth Syst. Sci.*, 23, 1631–1652, <https://doi.org/10.5194/nhess-23-1631-2023>, 2023.
- 505 Dahlhaus, P. G. and Miner, A. S.: Implementing the AGS Landslide Risk Management Guidelines in a Municipal Planning
506 Scheme: A Case Study in the Colac Otway Shire, Victoria, *Aust. Geomech. J.*, 37, 199–211,
507 <https://doi.org/10.3316/informit.810565236231586>, 2002.
- 508 DHI: MIKE SHE, an integrated hydrological modeling system: User guide, 2007.
- 509 Di Giammarco, P., Todini, E., and Lamberti, P.: A conservative finite elements approach to overland flow: the control
510 volume finite element formulation, *J. Hydrol.*, 175, 267–291, [https://doi.org/10.1016/S0022-1694\(96\)80014-X](https://doi.org/10.1016/S0022-1694(96)80014-X), 1996.
- 511 Edwards, J., Tickell, S.J., Willocks, A.J., Eaton, A.R., King, R.L., and Bourton, S.: Colac 1:250 000 geological map (Second
512 Edition), *Geol. Surv. of Vic.*, DENR, Victoria, Australia, Map MP-M-11614, 1996.
- 513 Fontúrbel, M. T., Barreiro, A., Vega, J. A., Martín, A., Jiménez, E., Carballas, T., Fernández, C., and Díaz-Raviña, M.:
514 Effects of an experimental fire and post-fire stabilization treatments on soil microbial communities, *Geoderma*, 191, 51–60,
515 <https://doi.org/10.1016/j.geoderma.2012.01.037>, 2012.
- 516 Freund, M., Henley, B. J., Karoly, D. J., Allen, K. J., and Baker, P. J.: Multi-century cool- and warm-season rainfall
517 reconstructions for Australia’s major climatic regions, *Clim. Past.*, 13, 1751–1770, <https://doi.org/10.5194/cp-13-1751-2017>,
518 2017.
- 519 Galang, M. A., Markewitz, D., and Morris, L. A.: Soil phosphorus transformations under forest burning and laboratory heat
520 treatments, *Geoderma*, 155, 401–408, <https://doi.org/10.1016/j.geoderma.2009.12.026>, 2010.
- 521 Gartner, J. E., Cannon, S. H., Santi, P. M., and Dewolfe, V. G.: Empirical models to predict the volumes of debris flows
522 generated by recently burned basins in the western U.S., *Geomorphology*, 96, 339–354,
523 <https://doi.org/10.1016/j.geomorph.2007.02.033>, 2008.
- 524 Geoscience Australia: Digital Elevation Model (DEM) of Australia derived from LiDAR 5 Metre Grid, Geoscience Australia
525 [data set], <https://doi.org/10.26186/89644>, 2015.



- 526 Giglio, L., Randerson, J. T., and van der Werf, G. R.: Analysis of daily, monthly, and annual burned area using the fourth-
527 generation global fire emissions database (GFED4), *J. Geophys. Res. Biogeosci.*, 118, 317–328,
528 <https://doi.org/10.1002/jgrg.20042>, 2013.
- 529 Giovannini, G., Lucchesi, S., and Giachetti, M.: Effect of heating on some physical and chemical parameters related to soil
530 aggregation and erodibility, *Soil Sci.*, 146, 255, <https://doi.org/10.1097/00010694-198810000-00006>, 1988.
- 531 Giovannini, G.: The effect of fire on soil quality, in: *Soil erosion as a consequence of forest fires*, edited by: Sala, M. and
532 Rubio, J.L., Geofoma Ediciones, Logrono, 15-27, 1994.
- 533 Goudie, A. S., Allison, R. J., and McLaren, S. J.: The relations between modulus of elasticity and temperature in the context
534 of the experimental simulation of rock weathering by fire, *Earth Surf. Process. Landf.*, 17, 605–615,
535 <https://doi.org/10.1002/esp.3290170606>, 1992.
- 536 Green, W. H. and Ampt, G. A.: *Studies on Soil Physics.*, *J. Agric. Sci.*, 4, 1–24, <https://doi.org/10.1017/S0021859600001441>,
537 1911.
- 538 Isbell, R. F. (Eds.): *The Australian Soil Classification*, Second Edition, CSIRO publishing, Clayton South VIC, Australia,
539 141 pp., ISBN 148630463X, 2016.
- 540 Japanese Association of Groundwater Hydrology: *Simulation of groundwater flow and solute transport*. Beijing: Japanese
541 Association of Groundwater Hydrology, 2010.
- 542 Kinzelbach, W.: *Groundwater Modelling: An Introduction with Sample Programs in BASIC*, Elsevier, 345 pp., 1986.
- 543 Lainas, S., Sabatakakis, N., and Koukis, G.: Rainfall thresholds for possible landslide initiation in wildfire-affected areas of
544 western Greece, *Bull Eng Geol Environ.*, 75, 883–896, <https://doi.org/10.1007/s10064-015-0762-5>, 2016.
- 545 Lanini, J. S., Clark, E. A., and Lettenmaier, D. P.: Effects of fire-precipitation timing and regime on post-fire sediment
546 delivery in Pacific Northwest forests, *Geophys. Res. Lett.*, 36, 1, <https://doi.org/10.1029/2008GL034588>, 2009.
- 547 Lei, M., Cui, Y., Ni, J., Zhang, G., Li, Y., Wang, H., Liu, D., Yi, S., Jin, W., and Zhou, L.: Temporal evolution of the
548 hydromechanical properties of soil-root systems in a forest fire in China, *Sci. Total Environ.*, 809, 151165,
549 <https://doi.org/10.1016/j.scitotenv.2021.151165>, 2022.
- 550 Linforth, D. J.: The climate of the Otway region, *Proc. R. Soc. Vic.*, 89, 61-68,
551 <https://www.cabidigitallibrary.org/doi/full/10.5555/19780772309>, 1977.
- 552 Liu, T., McGuire, L. A., Wei, H., Rengers, F. K., Gupta, H., Ji, L., and Goodrich, D. C.: The timing and magnitude of
553 changes to Hortonian overland flow at the watershed scale during the post-fire recovery process, *Hydrol. Process.*, 35,
554 e14208, <https://doi.org/10.1002/hyp.14208>, 2021.
- 555 Mallik, A. U., Gimingham, C. H., and Rahman, A. A.: Ecological Effects of Heather Burning: I. Water Infiltration, Moisture
556 Retention and Porosity of Surface Soil, *J. Ecol.*, 72, 767–776, <https://doi.org/10.2307/2259530>, 1984.
- 557 Mataix-Solera, J., Cerdà, A., Arcenegui, V., Jordán, A., and Zavala, L. M.: Fire effects on soil aggregation: A review, *Earth-*
558 *Sci. Rev.*, 109, 44–60, <https://doi.org/10.1016/j.earscirev.2011.08.002>, 2011.



- 559 May, C. L. and Gresswell, R. E.: Processes and rates of sediment and wood accumulation in headwater streams of the
560 Oregon Coast Range, USA, *Earth Surf. Process. Landf.*, 28, 409–424, <https://doi.org/10.1002/esp.450>, 2003.
- 561 Mein, R. G. and Larson, C. L.: Modeling infiltration during a steady rain, *Water Resour. Res.*, 9, 384–394,
562 <https://doi.org/10.1029/WR009i002p00384>, 1973.
- 563 Meyer, G. A., Pierce, J. L., Wood, S. H., and Jull, A. J. T.: Fire, storms, and erosional events in the Idaho batholith, *Hydrol.*
564 *Process.*, 15, 3025–3038, <https://doi.org/10.1002/hyp.389>, 2001.
- 565 Montgomery, D. R. and Dietrich, W. E.: A physically based model for the topographic control on shallow landsliding, *Water*
566 *Resour. Res.*, 30, 1153–1171, <https://doi.org/10.1029/93WR02979>, 1994.
- 567 Moody, J. A., Shakesby, R. A., Robichaud, P. R., Cannon, S. H., and Martin, D. A.: Current research issues related to post-
568 wildfire runoff and erosion processes, *Earth-Sci. Rev.*, 122, 10–37, <https://doi.org/10.1016/j.earscirev.2013.03.004>, 2013.
- 569 Neary, D. G., Ryan, K. C., and DeBano, L. F.: Wildland fire in ecosystems: effects of fire on soils and water, *Gen. Tech.*
570 *Rep. RMRS-GTR-42-vol. 4*, U.S. Department of Agriculture, Forest Service, Rocky Mountain Research Station, Ft. Collins,
571 CO, 250 pp, <https://doi.org/10.2737/RMRS-GTR-42-V4>, 2005.
- 572 Ng, C. W. W. and Menzies, B. (Eds.): *Advanced Unsaturated Soil Mechanics and Engineering*, 1st Edition, CRC Press,
573 London, 712 pp., <https://doi.org/10.1201/9781482266122>, 2014.
- 574 Nguyen, V. T., Wakai, A., Sato, G., Viet, T. T., and Kitamura, N.: Simple Method for Shallow Landslide Prediction Based
575 on Wide-Area Terrain Analysis Incorporated with Surface and Subsurface Flows, *Nat. Hazards Rev.*, 23, 04022028,
576 [https://doi.org/10.1061/\(ASCE\)NH.1527-6996.0000578](https://doi.org/10.1061/(ASCE)NH.1527-6996.0000578), 2022.
- 577 Noske, P. J., Lane, P. N. J., Nyman, P., Van der Sant, R. E., and Sheridan, G. J.: Predicting post-wildfire overland flow using
578 remotely sensed indicators of forest productivity, *Hydrol. Process.*, 36, e14769, <https://doi.org/10.1002/hyp.14769>, 2022.
- 579 Ozaki, T., Wakai, A., Watanabe, A., Cai, F., Sato, G., and Kimura, T.: A simplified model for the infiltration of rainwater in
580 natural slope consisting of fine sands, *J. of the Jpn. Landslide Soc.*, 58, 57–64, <https://doi.org/10.3313/jls.58.57>, 2021.
- 581 Pereira, P., Cerdà, A., Úbeda, X., Mataix-Solera, J., and Rein, G.: Fire Effects on Soil Properties, *Csiro Publishing*, 756 pp.,
582 2019.
- 583 Pereira, P., Úbeda, X., Mataix-Solera, J., Martin, D., Oliva, M., and Novara, A.: Short-term spatio-temporal spring grassland
584 fire effects on soil colour, organic matter and water repellency in Lithuania, *Soil System Science* [preprint],
585 <https://doi.org/10.5194/seed-5-2119-2013>, 22 November 2013.
- 586 Rawls, W. J., D. L. Brakensiek, and N. Miller: Green-Ampt infiltration parameters from soils data, *J. Hydraul. Eng.*, 109,
587 62–70, [https://doi.org/10.1061/\(ASCE\)0733-9429\(1983\)109:1\(62\)](https://doi.org/10.1061/(ASCE)0733-9429(1983)109:1(62)), 1983.
- 588 Rossel, R. A. V., Chen, C., Grundy, M., Searle, R., Clifford, D., Odgers, N., Holmes, K., and Kidd, D.: Clay (3" resolution) -
589 Soil and Landscape Grid National Soil Attribute Maps, *CSIRO* [data set], <https://doi.org/10.4225/08/546EEE35164BF>,
590 2014.
- 591 Saulnier, G.-M., Beven, K., and Obléd, C.: Including spatially variable effective soil depths in TOPMODEL, *J. Hydrol.*, 202,
592 158–172, [https://doi.org/10.1016/S0022-1694\(97\)00059-0](https://doi.org/10.1016/S0022-1694(97)00059-0), 1997.



- 593 Shakesby, R. A. and Doerr, S. H.: Wildfire as a hydrological and geomorphological agent, *Earth-Sci. Rev.*, 74, 269–307,
594 <https://doi.org/10.1016/j.earscirev.2005.10.006>, 2006.
- 595 Sidle, R. C. and Ochiai, H.: Introduction and Overview of Landslide Problems, in: *Landslides: Processes, Prediction, and*
596 *Land Use*, edited by: Sidle, R.C. and Ochiai, H., American Geophysical Union (AGU), 1–22,
597 <https://doi.org/10.1002/9781118665954.ch1>, 2006.
- 598 Soto, B., Benito, E., and Diaz-Fierros, F.: Heat-Induced Degradation Processes in Forest Soils, *Int. J. Wildland Fire.*, 1, 147–
599 152, <https://doi.org/10.1071/wf9910147>, 1991.
- 600 Specht, R. L.: Vegetation, in: *The Australian Environment*, edited by: Leeper, G.W., Melbourne University Press,
601 Melbourne, Australia, 44–67, 1970.
- 602 Spittler, T. E. and Wagner, D. L.: Geology and slope stability along highway 50, *Calif. Geol.*, 51, 3–14, 1998.
- 603 Staley, D. M., Negri, J. A., Kean, J. W., Laber, J. L., Tillery, A. C., and Youberg, A. M.: Prediction of spatially explicit
604 rainfall intensity–duration thresholds for post-fire debris-flow generation in the western United States, *Geomorphology*, 278,
605 149–162, <https://doi.org/10.1016/j.geomorph.2016.10.019>, 2017.
- 606 Standards Australia: AS 1289.3.6.1-2009-Methods of Testing Soils for Engineering Purposes-Soil Classification Tests-
607 Determination of Particle Size Distribution of a Soil – Standard Method of Analysis by Sieving, Standards Australia, 2009.
- 608 State Government of Victoria: Review of the initial response to the 2015 Wye River - Jamieson Track fire, IGEM reports,
609 State Government of Victoria, Melbourne, Australia, 56 pp., [https://www.igem.vic.gov.au/publications/igem-reports/review-](https://www.igem.vic.gov.au/publications/igem-reports/review-of-the-initial-response-to-the-2015-wye-river-jamieson-track-fire)
610 [of-the-initial-response-to-the-2015-wye-river-jamieson-track-fire](https://www.igem.vic.gov.au/publications/igem-reports/review-of-the-initial-response-to-the-2015-wye-river-jamieson-track-fire), 2016.
- 611 Varela, M. E., Benito, E., and Keizer, J. J.: Influence of wildfire severity on soil physical degradation in two pine forest
612 stands of NW Spain, *CATENA*, 133, 342–348, <https://doi.org/10.1016/j.catena.2015.06.004>, 2015.
- 613 Wakai, A., Hori, K., Watanabe, A., Cai, F., Fukazu, H., Goto, S., and Kimura, T.: A simple prediction model for shallow
614 groundwater level rise in natural slopes based on finite element solutions, *J. of the Jpn. Landslide Soc.*, 56, 227–239,
615 <https://doi.org/10.3313/jls.56.227>, 2019.
- 616 WGCMA: Soil Erosion Management Plan, Report, West Gippsland Catchment Management Authority, 132 pp., 2008.
- 617 Wieting, C., Ebel, B. A., and Singha, K.: Quantifying the effects of wildfire on changes in soil properties by surface burning
618 of soils from the Boulder Creek Critical Zone Observatory, *J. Hydrol.-Reg. Stud.*, 13, 43–57,
619 <https://doi.org/10.1016/j.ejrh.2017.07.006>, 2017.
- 620 Wondzell, S. M. and King, J. G.: Postfire erosional processes in the Pacific Northwest and Rocky Mountain regions, *For.*
621 *Ecol. Manage.*, 178, 75–87, [https://doi.org/10.1016/S0378-1127\(03\)00054-9](https://doi.org/10.1016/S0378-1127(03)00054-9), 2003.
- 622 Zhu, Y., Ishikawa, T., Siva Subramanian, S., and Luo, B.: Simultaneous analysis of slope instabilities on a small catchment-
623 scale using coupled surface and subsurface flows, *Eng. Geol.*, 275, 105750, <https://doi.org/10.1016/j.enggeo.2020.105750>,
624 2020.